Accepted Manuscript

Autopsy of an eruptive phase of Tungurahua volcano (Ecuador) through coupling of seismo-acoustic and SO$_2$ recordings with ash characteristics

J. Battaglia, S. Hidalgo, B. Bernard, A. Steele, S. Arellano, K. Acuña

Please cite this article in press as: Battaglia, J., et al. Autopsy of an eruptive phase of Tungurahua volcano (Ecuador) through coupling of seismo-acoustic and SO$_2$ recordings with ash characteristics. *Earth Planet. Sci. Lett.* (2019), https://doi.org/10.1016/j.epsl.2019.01.042

Highlights

- Eruptive dynamics characterized by seismicity, SO_2 degassing and ash componentry.
- Conduit conditions explored through multiparametric time series.
- Violent Strombolian vs. Vulcanian eruptive dynamics at Tungurahua volcano.
- Presence of a two magma waxing-waning cycles during a single eruptive phase.

1 **Autopsy of an eruptive phase of Tungurahua volcano**

2 **(Ecuador) through coupling of seismo-acoustic and SO₂**

3 **recordings with ash characteristics**

4

5 **J. Battaglia [1,*], S. Hidalgo [2], B. Bernard [2], A. Steele [3,2], S. Arellano [4], K. Acuña [2]**

6

7 [1] Université Clermont Auvergne, CNRS, IRD, OPGC, Laboratoire Magmas et Volcans, F-

8 63000, Clermont-Ferrand, France.

9 [2] *Instituto Geofísico Escuela Politécnica Nacional, Ladrón de Guevara E11-253 y Andalucía,*

10 *Quito, Ecuador.*

11 [3] *UCL Hazard Centre, Department of Earth Sciences, UCL, Gower St, London WC1E 6BT,*

12 *UK.*

13 [4] *Department of Space, Earth and Environment, Chalmers University of Technology,*

14 *Göteborg, Sweden.*

15 *Corresponding author. E-mail: j.battaglia@opgc.fr; tel:+33 473346779*

16

17 **Abstract**

18 Eruption style and dynamics are controlled by various parameters including magma supply

19 rate, magma viscosity, volatile content, and the permeability of the conduit. Rapid changes of

20 these parameters can significantly modify the hazards associated to the eruption processes and

21 understanding their relationship with multiparametric geophysical monitoring data can greatly

22 improve our forecasting capacities. From 2008 to 2016, volcanic activity at Tungurahua was

23 characterized by eruptive phases separated by episodes of quiescence. These phases displayed

24 great variability of eruptive patterns including Vulcanian and Strombolian explosions, low

25 pyroclastic fountaining, continuous or sporadic ash emissions and passive degassing. We use

26 the comparison between geophysical data (seismic, acoustic and SO_2 emission), recorded by

27 permanent monitoring networks, and the characteristics of the emitted ash to track changes in

28 eruption dynamics during an eruptive phase that lasted from late December 2009 to March

29 2010. We show that the correlation between the analyzed parameters allows imaging and

30 interpretation of the conditions at the vent. At Tungurahua, these conditions can rapidly

31 change at the time scale of a single eruptive phase, corresponding to various degrees of

32 opening, plugging and permeability of the conduit. Two magma intrusions could be identified

33 during a single eruptive phase showing transitions between violent Strombolian and

34 Vulcanian activity. Changes in the componentry of the analyzed ash samples, together with

35 the geophysical data, nicely highlight these evolutions. Studying these parameters

36 simultaneously provides a unique insight into the physical processes controlling superficial

37 volcanic activity and offers a potential tool for better understanding volcanoes and detecting

38 changes in their activity. The joint interpretation of multiparametric data which we propose is

39 potentially applicable to multiple andesitic volcanoes.

40

41 **1. Introduction**

42 Stratovolcanoes with long-lasting eruptive cycles, such as Tungurahua (Ecuador), Sakurajima

43 (Japan), Semeru (Indonesia), Soufrière Hills (West Indies, United Kingdom) or Popocatepetl

44 (Mexico), among others, pose a significant threat to local populations for three main reasons.

45 1) They constantly expose local populations to variable amounts of ash that can create chronic

46 health diseases (Baxter et al., 2014) and have long-term impacts on livelihoods (Few et al.,

47 2017). 2) Continuous accumulation of pyroclastic material on the flanks of the volcanic

48 edifice promotes the formation of rain-triggered lahars (Jones et al., 2015). 3) Local

49 authorities and populations are used to the more frequent low activity of the volcano and

50 might underestimate or overrule the potential impacts of the less frequent larger eruptions

51 (Mothes et al., 2015). A recent example is the June 2018 eruption of Fuego volcano

52 (Guatemala) that caused the death of at least 198 people (INACIF, 2019). During long-lasting

53 eruptions, the eruptive dynamics can rapidly shift from low explosive activity to high

54 explosive activity that translates into a substantial increase of the volcanic threat (Hidalgo et

55 al., 2015). These variations in surface activity are typically controlled by the characteristics of

56 the magma, such as composition, viscosity, permeability, bubble and crystal contents

57 (Cashman and McConnell, 2005; Melnik et al., 2005; Heap et al., 2015), the conditions at the

58 vent (i.e. open or closed) (Diller et al., 2006), the geometry of the conduit (Vitturi et al., 2008)

59 and the magma discharge rate (Cassidy et al., 2015; Bonadonna et al., 2016). Some of these

60 parameters can be quantitatively determined afterwards by conducting a precise analysis of

61 volcanic products like pyroclasts and/or lava (Wright et al., 2012; Gurioli et al., 2015).

62 However, the combined analysis of continuous geophysical signals permanently recorded by

63 multiparametric monitoring networks can give, in near real-time, at least qualitative insights

64 into the volcano behavior and help to forecast eruptive events (Ripepe et al., 2002, 2005).

65 Accurately imaging the evolution of eruptive dynamics through geophysical observations

66 ideally requires multiparametric monitoring systems including seismic, acoustic, geodetic,

67 thermal, geochemical, IR measurements, and visual observations.

68

69   Tungurahua (5023 m a.s.l.) is an andesitic stratovolcano located in Central Ecuador. It has an

70   eruptive recurrence interval of 80-90 years (Le Pennec et al., 2008). The most recent eruptive

71   cycle started in September 1999 and lasted until March 2016, with a major VEI3 paroxysm in

72   August 2006 (Eychenne et al., 2012). Tungurahua, as many other andesitic volcanoes,

73   displays various types of eruption styles: continuous to sporadic gas and ash emissions,

74   individual explosions with ejecta of blocks, low pyroclastic fountaining, violent explosions

75   producing pyroclastic density currents, and lava flows (Arellano et al., 2008; Samaniego et

76   al., 2011; Eychenne et al., 2012; Hall et al., 2015; Hidalgo et al., 2015). Pyroclastic

77   fountaining (e.g. Branney and Kokelaar, 2002) is different from spattering or lava fountaining

78   given that the pyroclasts are already solid in the gas jet. This term is more appropriate to

79   describe the activity at Tungurahua, as pointed out by Bernard (2018). There is an extensive

80   literature on Tungurahua's recent eruptive cycle focused on seismo-acoustic activity (Johnson

81   et al., 2005; Kumagai et al., 2010; Kim et al., 2014; Bell et al., 2017), degassing (Arellano et

82   al., 2008; Hidalgo et al., 2015), ground deformation (Champenois et al., 2014; Neuberg et al.,

83   2018), and eruption products (Samaniego et al., 2011; Wright et al., 2012; Eychenne et al.,

84   2012; Douillet et al., 2013; Eychenne et al., 2013; Hall et al., 2015; Bernard et al., 2016).

85   However, none of this research uses more than two methods to characterize the activity.

86   Furthermore, this literature is mostly focused on large events, such as the 2006 eruption, or

87   long periods of activity. Smaller events (VEI≤2) are mostly neglected. This last comment can

88   also apply in general to most of literature in volcanology.

89

90   For this study, we use seismic, acoustic, and SO_2 emission data to characterize the eruption

91   mechanisms during a phase of eruptive activity, which occurred from December 2009 to

92   March 2010. During this phase, Tungurahua exhibited a wide range of eruptive processes

93 including passive degassing, continuous ash venting and transient volcanic Strombolian and

94 Vulcanian explosions. We compare geophysical parameters with visual observations of the

95 surface activity reported by the Instituto Geofísico of Escuela Politécnica Nacional (IG-EPN)

96 and with diverse characteristics (geochemistry, mineralogy, componentry and grain-size

97 distribution) of ash samples collected throughout this eruptive phase. We use these

98 comparisons to propose a model of the temporal evolution of the eruption and determine the

99 vent conditions. The correlations highlighted in this paper can be used to follow and forecast

100 rapid changes in eruptive dynamics at andesitic volcanoes that show transitions between

101 emissive and explosive behaviors.

102

103 **2. Quantification of geophysical parameters and ash characterization**

104 **2.1 Seismic, acoustic and SO$_2$ emission quantification**

105 Tungurahua is monitored by the IG-EPN whose monitoring network includes five short-

106 period and five broadband seismic stations coupled with acoustic sensors (Kumagai et al.,

107 2010), and three permanent scanning-DOAS instruments (Novac-I, Galle et al., 2010). The

108 location of these instruments is shown in Figure 1. We examined the seismic, acoustic and

109 SO$_2$ data recorded during the eruptive sequence, which started on December 30, 2009 and

110 lasted until March 4, 2010. The seismicity of Tungurahua includes a great variety of signals

111 related to eruptive activity including explosion quakes generated by individual explosions but

112 also various types of tremors and chugging signals related to longer-duration venting (Figure

113 2). To quantify both short- and long-term variations we proceeded in two ways.

114

115 We first quantified the acoustic and seismic energies of large individual explosions. For this

116 purpose, we used data from the broadband and acoustic sensors. For each explosion with an

117 acoustic peak-to-peak amplitude greater than 45 Pa at reference station BMAS located 5.5 km

118 from the summit (equivalent to 100 Pa at 1 km from the vent as mentioned by Hidalgo et al.,

119 2015), we calculated the seismic and acoustic energies at each station using the formulas

120 proposed by Johnson and Aster (2005), namely:

121

122
$$E_{\text{acoustic}} = \frac{2\pi \; r^2}{\rho_{\text{atmos}} c_{\text{atmos}}} \int \Delta P(t)^2 dt \quad (1)$$

123

124 where E_{acoustic} is the acoustic energy (J), r is the distance from the station to the vent (between

125 4695 and 6341 m depending on station), ρ_{atmos} is the atmospheric density (between 0.7278 and

126 0.7878 kg/m³), c_{atmos} is the typical infrasound wave velocity at the average elevation of the

127 stations (339.2 m/s), $\Delta P(t)$ is the excess acoustic pressure measured by the instrument. And:

128

129
$$E_{\text{seismic}} = 2\pi r^2 \rho_{\text{earth}} c_{\text{earth}} \frac{1}{A} \int S^2 \; U(t)^2 dt \quad (2)$$

130

131 where E_{seismic} is the seismic energy (J), ρ_{earth} is the volcano density (2380 kg/m³), c_{earth} is the

132 P-wave velocity (3500 m/s), A is the attenuation factor (between 0.7963 and 0.8305), S is the

133 site response (1 for all stations), $U(t)$ is the particle velocity (m/s) measured by the

134 seismometer.

135

136 For each event, average seismic and acoustic energies were estimated by taking the mean

137 value of respective energies calculated at the four less noisy stations (BMAS, BPAT, BRUN

138 and BBIL, see Figure 1), assuming a fixed location at the vent surface for all explosion

139 sources. Energies were then summed up on a daily basis to obtain cumulative seismic (SEE)

140 and acoustic (AEE) explosion energies. Calculations show that AEE is generally about 100

141 times higher than SEE and therefore, for comparison, we refer to a reference value of 100 for

142 the AEE/SEE ratio. A total of 521 explosions were identified based on these criteria. The

143 presence of these high-energy explosions allowed the distinction among High Explosive

144 Activity (HEA) and Low Explosive Activity (LEA) periods (Hidalgo et al., 2015).

145

146 To estimate the amplitude of longer-term processes such as tremor, we calculated median

147 seismic amplitudes (MSA) over 10-minute sliding windows for the full short-period

148 frequency range (0.5-25 Hz). To obtain the median value of each window, we filter the

149 seismic signal with a 4-pole Butterworth filter, calculate the absolute value of the seismic

150 amplitudes and determine the median value of the amplitude distribution. For this, we used

151 the short-period station RETU (Figure 1), because it is the closest (3900 m asl) to the summit

152 and better reflects surface activity compared to more distant stations. However, when the

153 station was either saturated or experiencing technical problems, the time-series was completed

154 by using data from station BMAS, after scaling its MSA by an empirical factor estimated to

155 guarantee the continuity of the recordings. This empirical factor was calculated by matching

156 the amplitudes at RETU and BMAS when both stations were working properly. In figure 3,

157 we present MSA as values integrated over one-day windows. Finally, to specifically quantify

158 monochromatic or harmonic tremor we used the IG-EPN catalog, which characterizes this

159 type of activity by estimating the duration and mean amplitude of each burst identified by

160 frequency analysis. We calculated for each burst the product of these two parameters and

161 summed them on a daily basis. Because of differences in the calculation mode, results from

162 the quantification of monochromatic/harmonic tremor cannot directly be compared with the

163 daily cumulative MSA.

164

165 Scanning-DOAS instruments provide SO_2 emission rate measurements only during typically

166 ten hours of daylight at the volcano location and under good weather conditions, leading to

167 sometimes sparse time-series. To quantify the daily SO_2 emission with data from a dense

168 DOAS monitoring network, Hidalgo et al. (2015) proposed integrating the highest validated

169 SO_2 emission rate measurements among all stations to obtain a *daily observed mass of SO_2*,

170 rather than extrapolating the highest of the averages calculated for each station over the

171 available measurements obtained during the day. The daily-observed mass is originally

172 expressed in tons per 10 hours (the constant daily measurement duration), but can easily be

173 expressed in tons per day (t/d) by multiplying by a factor 2.4. This approach better takes into

174 account the daily-validated measurement duration (DVMD), i.e. the time of effective

175 detection of gas, which is usually high during eruptive phases and low during quiescence.

176 This method significantly improves long-term (i.e. yearly) correlation between SO_2 emission

177 and eruptive activity, as demonstrated by Hidalgo et al. (2015).

178

179 **2.2 Ash characterization**

180 The geophysical datasets were completed with direct observations on the eruptive dynamics

181 compiled by the Tungurahua Volcano Observatory (OVT for the Spanish acronym). We also

182 derived different characteristics from a total of eight samples of ash deposits collected by

183 volunteers on solar panels located at 6 to 8 km distance from the vent, on the WSW flank of

184 the volcano (under the most common wind direction) during the studied eruptive period.

185 These characteristics are: 1) bulk ash chemistry of major elements, 2) semi-quantitative

186 mineralogy, 3) componentry, and 4) grain-size distribution.

187

188 Bulk ash chemistry and semi-quantitative mineralogy were obtained at the Departamento de

189 Metalurgía Extractiva of the Escuela Politécnica Nacional (DEMEX-EPN). For the chemical

190 analysis we used an S8 TIGER High-end wavelength-dispersive X-ray fluorescence

191 (WDXRF) spectrometer with Spectra plus software. Analytical errors are around 1%. Semi-

192 quantitative mineralogy was obtained through X-ray diffraction (D8 Advance and Diffrac plus

193 software). Manual sieving and componentry were performed at the IG-EPN. The

194 componentry analysis followed the methodology described by Eychenne et al. (2012, 2013).

195 Over 300 grains were classified through optical microscopy and Secondary Electron

196 Microscopy (SEM) from at least four grain-size classes for each sample. Grain-size

197 distribution was obtained combining manual sieving for coarse fractions (-2 to 4 φ or D

198 between 16 and 0.063 mm, with $\varphi=-\log_2 D$ where D is the particle diameter in mm) and laser

199 diffraction (Horiba LA-9520V2) for the fine fractions (>4 φ or D<0.063 mm).

200

201 Bulk ash samples showed a homogenous andesitic composition throughout the two months of

202 eruption (SiO_2 = 57.81 ± 0.22%, K_2O = 1.73 ± 0.04%; 6 samples). Mineralogical assemblage

203 was characterized by plagioclase, clinopyroxene, orthopyroxene, olivine, and magnetite. This

204 assemblage was also constant for the 6 analyzed samples (Plagioclase = 61.0 ± 0.9%;

205 Clinopyroxene = 32.7 ± 1.9%; Orthopyroxene = 4.8 ± 1%; Olivine = 1.3 ± 0.5%; Magnetite =

206 0.2 ± 0.4%). These results are in agreement with previous analyses reported by Samaniego et

207 al. (2011).

208

209   Componentry analysis allowed the identification of eight classes (Figure 4). Four classes were

210   formed by juvenile material, two classes displayed accidental components, one comprised

211   only free crystals and the last class showed both juvenile and accidental features. Juvenile

212   components were identified as material exhibiting fresh vitreous shiny surface. They were

213   then divided according to their color (dark or honey) and vesicularity (dense or scoriaceous).

214   Accidental components were identified as material exhibiting more matte or opaque surfaces.

215   There were two accidental classes: 1) accidental oxidized fragments that showed a

216   homogeneous and penetrating reddish color, and 2) grey lithics that were generally dense and

217   slightly altered. Free crystals without attached groundmass were counted apart as it was

218   impossible to determine their origin with optical microscopy. Finally, an important class was

219   the vitreous oxidized fragments that exhibited both juvenile and accidental features. They

220   presented a very thin layer of rust on top of a shiny surface. This material was interpreted as

221   recycling of slightly altered, mostly fresh, material from the active crater (Acuña, 2017).

222   Significant variations were observed in the componentry (eight samples) throughout this

223   phase, with the beginning being characterized by honey color of mostly vesicular juvenile

224   material evolving through time to dark color of mostly dense juveniles. The detailed evolution

225   will be described in the next section together with the observed seismic and degassing

226   changes.

227

228   Grain-size distribution (six samples) was characterized by very fine to extremely fine ash (Mz

229    $= 3.38$-4.52 φ; $\sigma = 1.75$-2.43 φ; with Mz = mean $((\varphi_{16}+ \varphi_{50}+ \varphi_{84})/3)$ and σ = standard

230   deviation $((\varphi_{84}-\varphi_{16})/4+(\varphi_{95}-\varphi_{5})/6)$ as defined in Folk and Ward, 1957) and showed some

231   changes during this eruptive phase. All the samples showed bimodal distributions, with a

232   coarse mode between 1.8 and 2.9 φ (medium to fine ash), and a fine mode between 5.9 and

233   6.4 φ (extremely fine ash). In general, we observed coarsening of the coarse mode while the

234   fine mode remained rather constant throughout the eruption.

235

236   The ash data set does not mimic exactly the geophysical data because the ash samples were

237   both discontinuous and accumulated over inconsistent periods of time (few days to about a

238   week). This sampling creates an artificial smoothing of the changes in eruptive dynamics.

239   This is why in general geophysical data allow to better identify the different episodes but we

240   argue that petrological monitoring adds significant information to the conventional

241   geophysical monitoring and allows to better constrain the conduit processes (Gaunt et al.,

242   2016).

243

244   **3. Chronology of the eruptive phase**

245   The eruptive phase from December 2009 to March 2010 followed a period of almost six

246   months of quiescence. During this quiescent period, no surface activity was visually observed.

247   To describe eruptive activity at Tungurahua, Hidalgo et al. (2015) distinguished between LEA

248   (yellow background color in Figure 3) and HEA periods (orange in Figure 3). These last

249   periods are characterized by discrete, high-amplitude explosions, for which we have

250   calculated explosion energies (SEE and AEE), as described above. The eruptive phase

251   discussed here includes two periods of LEA separated by one period of HEA. We divide the

252   eruptive phase into six episodes whose beginning and end were defined according to changes

253   in the temporal evolutions of the geophysical parameters described above (Figure 3). The

254   evolution of componentry and grain-size of the ash is shown in Figure 4 and detailed for each

255   episode.

256

257   (a) *30 December 2009 – 3 January 2010: seismically silent magma ascent and degassing*. The

258   first signs of eruptive activity were observed late on 30 December 2009 with the occurrence

259   of a long period (LP) event followed by the emission of a small gas plume that reached a

260   height of ~300 m above the crater. A steady SO_2 emission rate (967 ± 221 t/d) was measured

261   during the following three days, with very small ash emission up to 1.5 km above the summit

262   (not seen by satellite instruments), accompanied by weak roaring sounds. This episode was

263   characterized by the almost complete absence of seismicity, even at station RETU, the closest

264   to the summit (2 km), except for a few small amplitude LP events. Despite this quiet onset,

265   visual observations inside the crater on 2 January indicated the presence of an incandescent

266   lava accumulation in the actively degassing crater. This feature was absent in November 2009.

267   This activity did not produce a significant amount of ash, leading only to very thin fallouts

268   restricted to the crater area. This prevented any ash sampling for this episode. The activity

269   began to change on 3 January with SO_2 emission increasing up to 3400 t/d.

270

271   (b) *3 - 10 January 2010: appearance of tremor*. After four days of degassing and weak ash

272   emissions, seismic signals related to venting processes appeared simultaneously with semi-

273   continuous ash plumes reaching up to 4.1 km above the crater (as reported by the Washington

274   VAAC) and weak pyroclastic fountaining. Few discrete explosions were recorded during this

275   episode. A progressive buildup of the MSA accompanied an irregular increase and

276   stabilization of SO_2 emissions, which averaged 3073 ± 1140 t/d during the episode. SO_2

277   individual measurements showed an increase in daily variability, indicating a more

278   discontinuous gas discharge, which is in agreement with the appearance of tremor pulses that

279   occasionally had large amplitudes (MSA peak on 7 January). Episodes of harmonic tremor

280 started on 7 January. This activity was associated with low-to-moderate intensity roaring

281 sound. During this episode the ash grain-size distribution was bimodal and fine-grained, as for

282 most of the eruption. Ash componentry was dominated (>85 %) by honey-color juvenile

283 fragments (mostly scoria), with some free crystals and a very small amount of accidental

284 material (grey lithics or oxidized fragments) and dark-color juvenile (two samples 06/01 in

285 Figure 4).

286

287 (c) *11 - 15 January 2010: appearance of larger explosions*. On 11 January, a major change

288 was observed in eruptive activity with the appearance of larger explosions with typical canon-

289 like shot sounds, sometimes followed by high amplitude tremor. This transition was not

290 accompanied by any marked increase in the flux of SO_2, which remained stable around 2760

291 $\pm$ 1516 t/d. This highly explosive activity, which lasted for five days, showed strong seismic

292 energy partitioning (AEE/SEE<<100). The superficial activity was characterized by

293 explosions ejecting ballistics, followed by low pyroclastic fountaining. This activity was

294 associated with sustained ash plumes (typically 3 km-high, and up to 5 km-high) and

295 moderate-to-high intensity roaring sound. Harmonic tremor was recorded throughout the

296 episode and almost vanished afterwards (Figure 3). Moderate to strong ash fallouts occurred

297 during this episode. The change of eruptive activity was directly recorded in the componentry

298 of the ash sample while the grain-size distribution remained unchanged and fine-grained

299 (sample 12/01). The amount of honey-color juvenile material dropped to ~37% while the

300 amount of dark-color and vitreous oxidized particles rose to 34 and 20% respectively. Free

301 crystals and grey lithics remained very scarce (Figure 4).

302

303   (d) *16 - 23 January 2010: drop of explosive activity*. A drop in explosive activity (SEE and

304   AEE) was observed on 16 January coinciding with a decrease and stabilization of tremor

305   amplitude as seen in the MSA. A few less energetic explosions remained with a ratio

306   AEE/SEE>100. This drop in seismicity was, however, only accompanied by a very small

307   reduction of SO_2 emissions (2495 ± 887 t/d). Pyroclastic fountaining and quasi-continuous

308   gas and ash emissions reaching up to 3 km above the summit were observed, associated with

309   moderate intensity roaring sounds and small-to-moderate intensity ash fallouts, whose

310   juvenile fraction was dominated by dark-color and scoriaceous material (sample 20/01).

311

312   (e) *24 January - 24 February 2010: increase in larger explosions*. Large explosions resumed

313   progressively from 24 January with an energy increasing irregularly until 11 February before

314   decaying towards the end of the episode. This change was correlated with an intensification of

315   roaring and canon-shot-like sounds, an increase of column height (typically 2 km and up to 4

316   km above the summit) and ash content of the emissions. Compared to episode (c), the daily

317   number of large explosions was similar but the SEE was significantly lower and the AEE

318   higher, resulting in a ratio AEE/SEE>100 during most of the episode, similarly to episode (d).

319   A decrease of this ratio (<100) was observed during the end of the episode, simultaneously

320   with the drop of both energies. Accompanying this activity, the MSA decreased smoothly

321   except for a short increase peaking around 5 February. These signals corresponded to a

322   progressive decrease of background tremor, which was replaced by occasional LPs or

323   explosions. Grain-size distribution showed a significant increase in the fine mode fraction

324   compared to previous episodes (Sample 6/02). During this episode, the SO_2 emission

325   displayed significant fluctuations with a globally decaying trend (1729 ± 1272 t/d), except for

326   a short-duration increase roughly synchronous with the one observed for the MSA and the

327   change in grain-size distribution (Sample 6/02). Small pyroclastic flows due to collapses of

328   the material accumulated near the vent occurred at the end of this episode. This was followed

329   by a slight coarsening of the ash grain-size. The ash componentry became clearly dominated

330   (>85 %) by dark-color juvenile fragments (samples 17 and 24/02). Also, interestingly, we

331   observed an increase of dense material compared to scoria.

332

333   (f) *25 February to 4 March 2010: dying out of the activity*. By 25 February, sporadic ash

334   emissions (less than 3 km-high) were observed with only minor seismic activity: a few

335   transient events including mostly LPs and no significant tremor. SO_2 was almost at

336   background levels observed during quiescence periods (78 ± 41 t/d). The small ash fallouts

337   during this episode showed a slight decrease of the amount of dark-color juvenile material

338   even though it still remained as the main component (>80%). The ash grain-size distribution

339   was also slightly finer-grained compared to the episode (e) mostly associated to a higher

340   amount of the fine sub-population mode (sample 07/03).

341

342   The average emission rate of SO_2 during the entire eruptive phase was 1807 ± 1394 t/d, which

343   is equivalent to a total gas release of about 120 kt of SO_2 to the atmosphere during the 65 days

344   of activity. We found average emissions of 2020 ± 1302 during HEA (45 days) and 1430 ±

345   1591 t/d during LEA (20 days). It could be argued that this difference reflects a real change in

346   gas emissions. A t'Student test of the difference between the averages of the two samples

347   (HEA and LEA daily measurements) resulted in a p-value of 0.08, meaning an 8% probability

348   of having observed a false difference by chance. However, we note that the size of our

349   samples is not large enough to derive a robust conclusion in a statistically significant sense.

350 The typical uncertainty of individual measurements is estimated at about 30% (see Galle et

351 al., 2010; Hidalgo et al., 2015).

352

353 **4. Discussion**

354 The comparison of the different geophysical time series with visual observations of

355 superficial activity and ash characteristics provides unique information about the eruptive

356 dynamics and processes occurring in the conduit. We discuss and interpret the parameters for

357 each episode to recompose the temporal evolution of the eruptive phase. The sketches shown

358 in Figure 5 illustrate this evolution.

359

360 (a) *Open conduit, silent magmatic ascent with free magma degassing*

361 The progressive and seismically silent appearance of gas during episode (a) can be interpreted

362 as a new batch of magma reaching the surface through an open conduit, with SO_2 easily and

363 rapidly exsolving through a permeable ascending magmatic column. This corresponds to the

364 seemingly seismically silent emplacement of the lava observed in the crater on 2 January. This

365 lack of seismicity is rather uncommon, especially for magmas with a high viscosity. For

366 basaltic magmas, seismically silent lava outpouring from a shallow pocket has been reported

367 at Etna (Bonaccorso et al., 2006), and Eibl et al. (2017) reported silent magma transport at

368 Bardarbunga after dyke opening. At Tungurahua, the high temperature (~1000°C) of andesites

369 (58-59 wt.% SiO_2) and their high water content (5-6 wt.% H_2O) may result in a relatively low

370 viscosity magma (Samaniego et al., 2011; Andújar et al., 2017). Therefore, the slow

371 emplacement of a small volume of lava in the crater, originating from a shallow source, as

372 well as the fact that the closest station is located at about 2 km from the crater, could explain

373 the absence of recorded seismicity. The low ash content in the emissions was likely due to

374 passive reworking of ash driven by high gas pressure (Figure 5a). Our observations suggest

375 that when the conduit is open to magma transport, a seismically silent propagation of magma

376 is possible but not without generating SO_2 emission.

377

378 (b) *Removal of the blocky lava surface and deepening of the fragmentation surface*

379 The sustained degassing and low explosive activity may have resulted in the removal of part

380 of the blocky lava emplaced at the top of the conduit toward the end of episode (a). Such a

381 process may have lowered the pressure in the conduit, leading to an increase in the amount of

382 exsolved SO_2 as observed since 3 January. This type of depressurization-induced degassing

383 has been modeled by Girona et al. (2014). Higher gas exsolution could have led in turn to

384 magmatic fragmentation, which would have progressively depleted the upper part of the

385 magma column. This process would result in an increase in viscosity and density of the

386 remaining magma, ultimately generating a denser, less fluid and permeable zone in the

387 magma column. This is in agreement with the model proposed by Diller et al. (2006) based on

388 the 1997 Vulcanian activity of Soufrière Hills volcano, Montserrat. The progressive

389 appearance of tremor during episode (b) is in good agreement with the formation of a

390 rheological barrier or partial plug. Tremor or tremor bursts may be caused by resonances

391 induced in this barrier by the continuous or intermittent transit of gas through this denser

392 zone, based on similar mechanisms to those proposed by Ferrick et al. (1982) or Julian et al.

393 (1994) for the generation of tremor, for example. Preliminary locations obtained for eruptive

394 phases in 2014 with a dense seismic network (Battaglia et al., 2015), suggest that a large part

395 of volcanic sources (tremors, LPs, explosion quakes) may be located about 1 km below the

396 summit. This depth is in agreement with results found by Kumagai et al. (2010) and Kim et al.

397 (2014) for explosion sources at Tungurahua recorded respectively in May 2009 and May

398 2010. Since the source location appears to be relatively constant through time, we may

399 speculate that the barrier at the origin of tremors and explosions during our eruptive phase

400 was formed at about 1 km below the summit (800 m below the crater floor). The increase of

401 tremor amplitude may be related to the progressive narrowing of the resonating conduit or an

402 increase in gas flux and ash emissions. The occurrence of harmonic tremor during this episode

403 may be explained by specific geometries of the conduit during the formation of the dense

404 barrier, leading to specific dominant frequencies in a similar way to the clarinet model

405 proposed by Lesage et al. (2006) for Arenal volcano. The shallow activity (violent

406 Strombolian explosions, low pyroclastic fountaining and small ash plumes) might be

407 explained by the migration of volatiles through the low-viscosity magma in the upper part of

408 the conduit, leading to magmatic fragmentation and enhancing the growth of the plug. The

409 mostly vesiculated honey-color juvenile material would be the evidence of this shallow

410 magmatic fragmentation and rapid ascent of magma thought the conduit. Similar vesicular

411 material has been observed at Villarrica volcano and reported as golden pumice by Gurioli et

412 al. (2008).

413

414 (c) *Explosive activity during conduit cleaning, muffling effect and stiffening of the rheological barrier*

415 The appearance of large explosions during episode (c), without any large increase in the rate

416 of SO_2 degassing, suggests a transition in the way in which gas escapes rather than an increase

417 in the amount of exsolved gas. The barrier formed during episode (b) acts like a plug or valve

418 system during episode (c), leading to the accumulation and cyclic release of highly over-

419 pressured gases that trigger Vulcanian explosions. A similar mechanism is proposed by

420 Campion et al. (2018) for E2-type explosions at Popocatépetl volcano. Nevertheless, in this

421 last case the gas is unable to escape due to a rapid gravitational compaction of dome, while

422   we propose a densification of the magma due to the exsolution and loss of gas following the

423   model of Heap et al. (2015). Magma densification by gas loss and conduit plug formation

424   have also been modeled by Diller et al. (2006) and used to explain Vulcanian activity at

425   Soufrière Hills. These authors showed that a dense zone, a plug, could be produced at 750 m

426   depth, a depth similar to the one assumed in present work (800 m below the crater level).

427   During episode (c), the plug sits below already fragmented juvenile and old material, which

428   results in a muffling of acoustic waves and a ratio AEE/SEE<<100. Recycling of this material

429   in the ash column is evidenced by the drastic increase of vitreous oxidized material in the ash

430   componentry. Large explosions eject parts of this material as well as new magmatic foam and

431   gases released through the plug. Dark juvenile material shows a sharp increase at this time.

432   Similar dark dense material has also been reported in direct relation to Vulcanian explosions

433   at Colima volcano (Cassidy et al., 2015). Harmonic tremor is still generated, sometimes

434   following the occurrence of large explosions, and might be associated to the production of

435   honey-color juvenile material. These internal processes coincide with the strongest superficial

436   activity interpreted as a mixed dynamism between violent Strombolian, mainly characterized

437   by the dominance of honey-color juvenile components, and Vulcanian eruptive styles,

438   dominated by dark juveniles.

439

440   (d) *Open conduit and triggering of a second magmatic pulse*

441   After the partial or complete destruction of the plug, the conduit is partially open again during

442   episode (d). The pressure drop produced by the partial emptying of the conduit might have

443   triggered a new magmatic injection through a depressurization mechanism similar to that

444   proposed by Girona et al. (2014). The absence of chemical or mineralogical changes in the

445   subsequent eruptive products suggests that the source of this new injection is the same as the

446 one that occurred during episode (a). According to Samaniego et al. (2011), the magmatic

447 reservoir that fed the shallow system between 1999 and 2006 was located between 7.5 and 9.5

448 km below the summit. This arrival of new magma explains the sustained SO_2 degassing and

449 ash venting observed despite the clear decrease of superficial activity at the end of episode

450 (c). Mostly continuous tremor is recorded accompanying these SO_2 and ash emissions.

451 Starting with this episode, the smoothed SO_2 time-series roughly follows the MSA,

452 suggesting a common source process. Only a few significant explosions are observed which

453 may relate to the occasional formation of an impermeable zone near the free surface, as

454 supported by the AEE/SEE ratio (>100). Dark-color and honey-color juvenile material are

455 fairly equivalent during this episode.

456

457 (e) *Explosive events after conduit cleaning, followed by progressive stiffening of the plug*

458 *inside the conduit*

459 Episode (e) shows a new increase in the number of significant explosions, except that a high

460 AEE/SEE ratio (>100) is recorded during most of the episode, suggesting that the upper

461 conduit is less clogged in comparison to episodes b and c. In terms of magma supply, it can be

462 interpreted as composed of two sub-episodes, from 24 January to 4 February (e.i), and from 5

463 to 24 February (e.ii), repeating a waxing-waning sequence similar to the one which occurred

464 during episodes (b), (c) and (d). Therefore, (e.i) is interpreted as the increase of activity

465 caused by the arrival of new gas-rich magma. However, compared to (b), the presence of a

466 more efficient rheological barrier (plug) or a deeper level of fragmentation may explain the

467 occurrence of Vulcanian explosions in between of the dominating violent Strombolian activity

468 (Bernard, 2018). In contrast, (e.ii) would rather correspond to waning of the episode with

469 more "pure" Vulcanian activity, as shown by the seismo-acoutic ratios of explosions and the

470 clear increase in dense black juvenile components in the ash and the coarsening of the grain-

471 size dominant mode. The decrease in SO_2 emissions, explosion energies and MSA during

472 (e.ii) indicates a decreasing magma supply rate. This would lead to the progressive plugging

473 and obstruction of the conduit. Its progressive burial may then explain the decrease of the

474 AEE/SEE ratio (<100) observed toward the end of the episode.

475

476 (f) *Sealing of the system*

477 Finally, episode (f) corresponds to the final closing and sealing of the conduit with only

478 residual ash and gas being emitted. The characteristics of the ash are similar to those from

479 episode (e) with a small increase of oxidized material, recycled from the vent. The plug

480 emplaced at the end of the eruption was later broken at the beginning of the following

481 eruptive phase which started in May 2010 with Vulcanian explosions and moderate-size

482 pyroclastic flows (Kim et al., 2014; Hidalgo et al., 2015; Bernard, 2018).

483

484 The eruptive phase that we studied, displayed a wide spectrum of eruptive dynamics. We

485 interpret this diversity as being the result of variable conditions of opening or constriction of a

486 rheological barrier or plug in the conduit, additionally to variations in the magma supply rate.

487 Despite the morphological differences, Soufrière Hills volcano displayed similar dynamics

488 during its eruptive activity from 2005 to 2010, showing also ash venting and Vulcanian

489 explosions. At Soufrière Hills, Cole et al. (2014) explained the ash venting by short term

490 increases in the extrusion rate related to shear-induced fragmentation at the conduit margin.

491 Seismic tremor and ash componentry were similar to what we observed in episode (b). The

492 origin of Vulcanian explosions at Popocatepetl or Montserrat is ascribed respectively to the

493 self-collapse of the dome (Campion et al., 2018) and the sealing of the dome cracks, allowing

494 degassing, by precipitation of hydrothermal minerals (Edmonds et al., 2003). At Tungurahua,

495 the activity does not include the formation of domes and its Vulcanian explosions are more

496 similar to those observed at Sakurajima volcano (Watt et al., 2007). Hence, we argue that a

497 high-viscosity, high-density barrier inside the conduit is responsible for the occurrence of

498 Vulcanian explosions, following the experimental models proposed by Heap et al.

499 (2015), while the violent Strombolian activity is probably associated to a hotter less

500 degassed magma.

501

502 **5. Conclusions**

503 The comparison of seismic, acoustic and SO_2 gas emission time series recorded during the

504 December 2009 - March 2010 eruptive phase of Tungurahua volcano outlines diverse patterns

505 and correlations between the parameters. Based on this diversity, we identified 6 episodes

506 with different characteristics, which we interpret in terms of conduit conditions and magma

507 supply rate. During these episodes, degassing could freely occur without generating any

508 seismicity if the conduit was open. Tremor could be observed, including monochromatic

509 tremor if the conduit was (properly) constricted and larger Vulcanian explosions could occur

510 if it was occasionally or partially plugged. At some point, dynamics changed from continuous

511 degassing during ash venting and violent Strombolian activity to a degassing dominated by

512 Vulcanian explosions without any significant change in the amount of SO_2 emitted from the

513 vent.

514

515 We associate this variability to changes in the conduit and more specifically to the evolution

516 of a rheological barrier or plug which we assume to be about 1 km below the summit based on

517 locations of seismic sources. Vent conditions and fragmentation processes are also clearly

518 reflected in the ash componentry and to a lower degree in the grain-size distribution. Our

519 results suggest that the correlation of multiparametric data can highlight transitions in the

520 nature of superficial activity that can be confirmed through petrological monitoring. They also

521 outline geophysical patterns that allow to identify two waxing-waning cycles within the

522 eruptive phase produced by a second magmatic injection. The geophysical and petrological

523 signature of the two cycles was different as the conduit conditions evolved.

524

525 Comparing and correlating the different parameters allow making better interpretations of the

526 eruption evolution which is of major importance to improve hazard assessment. Our

527 interpretation patterns may be applied to most andesitic volcanoes independently of the

528 presence of plugs or domes which may act as shallow rheological barriers.

529

536

537 **WEB REFERENCES**

538   INACIF, http://www.inacif.gob.gt/index.php/component/content/article/89-

539 noticias/ultimas-noticias/116-actualizacion-de-los-datos-del-trabajo-realizado-por-personal-

540 del-inacif-en-atencion-a-la-emergencia-producida-por-la-erupcion-del-volcan-de-fuego

541 (accessed 17/1/2019)

542

BIBLIOGRAPHY

544 Acuña Mondragón, K.E., 2017. Análisis de las cenizas del Tungurahua (granulométrico, de componentes y químico) en la primera fase eruptiva de 2010 (enero-marzo). BSc Eng. project thesis, Escuela Politécnica Nacional, Quito (Ecuador), 144 p.

Andújar, J., Martel, C., Pichavant, M., Samaniego, P., Scaillet, B., Molina, I., 2017. Structure of the plumbing system at Tungurahua volcano, Ecuador: insights from phase equilibrium experiments on July-August 2006 eruption products. Journal of Petrology, 58(7), 1249-1278, https://doi.org/10.1093/petrology/egx054.

Arellano, S.R., Hall, M., Samaniego, P., Le Pennec, J.-L., Ruiz, A., Molina, I., Yepes, H., 2008. Degassing patterns of Tungurahua volcano (Ecuador) during the 1999–2006 eruptive period, inferred from remote spectroscopic measurements of SO_2 emissions. J. Volcanol. Geotherm. Res. 176(1), 151-162, https://doi.org/10.1016/j.jvolgeores.2008.07.007.

Battaglia, J., Hartmann, J., Hidalgo, S., Douchain, J.-M., Cordova, J., Alvarado, A., Ruiz, M., Parra, R., 2015. Location and waveform classification of seismicity at Tungurahua volcano (Ecuador) during the February and April 2014 eruptive phases. In 2015 AGU Fall Meeting.

Baxter, P.J., Searl, A.S., Cowie, H.A., Jarvis, D., Horwell, C.J., 2014. Evaluating the respiratory health risks of volcanic ash at the eruption of the Soufriere Hills Volcano, Montserrat, 1995 to 2010. *Geological Society, London, Memoirs 39*(1), 407-425, https://doi.org/10.1144/M39.22.

563   Bell, A. F., Hernandez, S., Gaunt, H. E., Mothes, P., Ruiz, M., Sierra, D., Aguaiza, S.,

564   2017. The rise and fall of periodic 'drumbeat' seismicity at Tungurahua volcano, Ecuador.

565   Earth Planet. Sci. Lett. *475*, 58-70, https://doi.org/10.1016/j.epsl.2017.07.030.

566   Bernard, J., Eychenne,J., Le Pennec, J.-L., Narvaez Rivadeneira, D., 2016. Mass budget

567   partitioning during explosive eruptions: insights from the 2006 paroxysm of Tungurahua

568   volcano, Ecuador, Geochem. Geophys. Geosyst. 17, https://doi.org/10.1002/2016GC006431.

569   Bernard, B., 2018. Rapid hazard assessment of volcanic ballistic projectiles using long-

570   exposure photographs: insights from the 2010 eruptions at Tungurahua volcano, Ecuador.

571   Volcanica 1(1), 49-61. doi: https://doi.org/10.30909/vol.01.01.4961.

572   Bonaccorso, A., Bonforte, A., Guglielmino, F., Palano, M., Puglisi, G., 2006. Composite

573   ground deformation pattern forerunning the 2004–2005 Mount Etna eruption. J. Geophys.

574   Res., Solid Earth *111*(B12), https://doi.org/10.1029/2005JB004206.

575   Bonadonna, C., Cioni, R., Costa, A. et al., 2016. MeMoVolc report on classification and

576   dynamics of volcanic explosive eruptions. Bull. Volcanol. 78(11), 84,

577   https://doi.org/10.1007/s00445-016-1071-y.

578   Branney, M.J., Kokelaar, B.P., 2002. Pyroclastic Density Currents and the Sedimentation of

579   Ignimbrites. Geological Society of London, 156 p. ISBN 978-1-86239-124-6.

580   Campion, R., Delgado-Granados, H., Legrand, D., Taquet, N., Boulesteix, T., Pedraza-

581   Espitía, S., Lecocq, T., 2018. Breathing and Coughing: The extraordinarily high degassing of

582   Popocatépetl volcano investigated with an SO_2 camera. Frontiers in Earth Science *6*, 163,

583   https://doi.org/10.3389/feart.2018.00163.

584   Cashman, K.V., McConnell, S.M., 2005. Multiple levels of magma storage during the 1980

585   summer eruptions of Mount St. Helens, WA. Bull. Volcanol. 68, 57-75,

586   https://doi.org/10.1007/s00445-005-0422-x.

587   Cassidy, M., Cole, P.D., Hicks, K.E., Varley, N.R., Peters, N., Lerner, A.H., 2015. Rapid

588   and slow: Varying magma ascent rates as a mechanism for Vulcanian explosions. Earth

589   Planet. Sci. Lett. *420*, 73-84, https://doi.org/10.1016/j.epsl.2015.03.025.

590   Champenois, J., Pinel, V., Baize, S., Audin, L., Jomard, H., Hooper, A., Alvarado, A.,

591   Yepes, H., 2014. Large-scale inflation of Tungurahua volcano (Ecuador) revealed by

592   Persistent Scatterers SAR interferometry. Geophys. Res. Lett. 41(16), 5821-5828,

593   https://doi.org/10.1002/2014GL060956.

594   Cole, P.D., Smith, P., Komorowski, J.-C., Alfano, F., Bonadonna, C., Stinton, A.,

595   Christopher, T., Odbert, H.M., Loughlin, S., 2014. Ash venting occurring both prior to and

596   during lava extrusion at Soufriere Hills Volcano, Montserrat, from 2005 to 2010. *Geological*

597   *Society, London, Memoirs*, *39*(1), 71-92.

598   Diller, K., Clarke, A.B., Voight, B., Neri, A., 2006. Mechanisms of conduit plug formation:

599   Implications for vulcanian explosions, Geophys. Res. Lett. 33(20),

600   https://doi.org/10.1029/2006GL027391.

601   Douillet, G.A., Pacheco, D.A., Kueppers, U., Letort, J., Tsang-Hin-Sun, È., Bustillos, J.,

602   Hall, M., Ramón, P., Dingwell, D.B., 2013. Dune bedforms produced by dilute pyroclastic

603   density currents from the August 2006 eruption of Tungurahua volcano, Ecuador. Bull.

604   Volcanol. 75(11), 762, https://doi.org/10.1007/s00445-013-0762-x.

605   Edmonds, M., Oppenheimer, C., Pyle, D.M., Herd, R.A., Thompson, G., 2003. SO_2

606   emissions from Soufrière Hills Volcano and their relationship to conduit permeability,

607   hydrothermal interaction and degassing regime. J. Volcanol. Geotherm. Res *124*(1-2), 23-43,

608   https://doi.org/10.1016/S0377-0273(03)00041-6.

609   Eibl, E.P., Bean, C.J., Vogfjörd, K.S., Ying, Y., Lokmer, I., Möllhoff, M., O'Brien, G.S.,

610   Pálsson, F., 2017. Tremor-rich shallow dyke formation followed by silent magma flow at

611   Bárðarbunga in Iceland. Nat. Geosci. *10*(4), 299, https://doi.org/10.1038/ngeo2906.

612   Eychenne, J., Le Pennec, J.-L., Troncoso, L., Gouhier, M., Nedelec J.-M., 2012. Causes

613   and consequences of bimodal grain-size distribution of tephra fall deposited during the August

614   2006 Tungurahua eruption (Ecuador). Bull. Volcanol. 74, 187-205.

615   https://doi.org/10.1007/s00445-011-0517-5.

616   Eychenne J., Le Pennec J.-L., Ramón P., Yepes H., 2013. Dynamics of explosive

617   paroxysms at open-vent andesitic systems: High-resolution mass distribution analyses of the

618   2006 Tungurahua fall deposit (Ecuador). Earth Planet. Sci. Lett. 361, 343–355,

619   https://doi.org/10.1016/j.epsl.2012.11.002.

620   Ferrick, M.G., Qamar, A., St. Lawrence, W.F., 1982. Source mechanism of volcanic tremor.

621   J. Geophys. Res. 87, 8675-8683.

622   Few, R., Armijos, M.T., Barclay, J., 2017. Living with Volcan Tungurahua: the dynamics of

623   vulnerability during prolonged volcanic activity. *Geoforum 80*, 72-81,

624   https://doi.org/10.1016/j.geoforum.2017.01.006.

625   Folk, R.L., Ward, W.C., 1957. Brazos river bar (Texas): a study of the significance of

626   grainsize parameters. J Sediment Petrol 27(1), 3-26.

627   Galle, B., Johansson, M., Rivera, C., Zhang, Y., Kihlman, M., Kern, C., Lehmann, T., Platt,

628   U., Arellano, S., Hidalgo, S., 2010. Network for Observation of Volcanic and Atmospheric

629   Change (NOVAC) - a global network for volcanic gas monitoring: network layout and

630 instrument description. J. Geophys. Res., Atmos 115(D5), 2156–2202, https://doi.org/10.1029/2009JD011823.

631

632 Gaunt, H.E., Bernard, B., Hidalgo, S., Proaño, A., Wright, H., Mothes, P., Criollo, E.,

633 Kueppers, U., 2016. Juvenile magma recognition and eruptive dynamics inferred from the

634 analysis of ash time series: The 2015 reawakening of Cotopaxi volcano. J. Volcanol.

635 Geotherm. Res. 328, 134-146, https://doi.org/10.1016/j.jvolgeores.2016.10.013.

636 Girona, T., Costa, F., Newhall, C., Taisne, B., 2014. On depressurization of volcanic

637 magma reservoirs by passive degassing. J. Geophys. Res., Solid Earth *119*(12), 8667-8687,

638 https://doi.org/10.1002/2014JB011368.

639 Gurioli, L., Harris, A.J.L., Houghton, B.F., Polacci, M., Ripepe, M., 2008. Textural and

640 geophysical characterization of explosive basaltic activity at Villarrica volcano. J. Geophys.

641 Res., Solid Earth *113*(B8), https://doi.org/10.1029/2007JB005328.

642 Gurioli, L., et al., 2015. MeMoVolc consensual document: a review of cross-disciplinary

643 approaches to characterizing small explosive magmatic eruptions. Bull. Volcanol. 77,

644 https://doi.org/10.1007/s00445-015-0935-x.

645 Hall, M.L., Steele, A.L., Bernard, B., Mothes, P.A., Vallejo, S.X., Douillet, G.A., Ramón,

646 P.A., Aguaiza, S.X., Ruiz, M.C., 2015. Sequential plug formation, disintegration by Vulcanian

647 explosions, and the generation of granular Pyroclastic Density Currents at Tungurahua

648 volcano (2013–2014), Ecuador. J. Volcanol. Geotherm. Res. 306, 90-103,

649 https://doi.org/10.1016/j.jvolgeores.2015.09.009.

650 Heap, M.J., Farquharson, J.I., Wadsworth, F.B., Kolzenburg, S., Russell, J.K., 2015.

651 Timescales for permeability reduction and strength recovery in densifying magma. Earth

652 Planet. Sci. Lett. 429, 223-233, https://doi.org/10.1016/j.epsl.2015.07.053.

653   Hidalgo, S., Battaglia, J., Arellano, S., Steele, A., Bernard, B., Bourquin, J., Galle, B.,

654   Arrais, S., Vásconez, F., 2015. SO_2 degassing at Tungurahua volcano (Ecuador) between 2007

655   and 2013: Transition from continuous to episodic activity. J. Volcanol. Geotherm. Res. 298, 1-

656   14, https://doi.org/10.1016/j.jvolgeores.2015.03.022.

657   Johnson, J.B., Aster, R.C., 2005. Relative partitioning of acoustic and seismic energy

658   during strombolian eruptions. J. Volcanol. Geotherm. Res. 148, 334-354,

659   https://doi.org/10.1016/j.jvolgeores.2005.05.002.

660   Jones, R., Manville, V., Andrade, D., 2015. Probabilistic analysis of rain-triggered lahar

661   initiation at Tungurahua volcano. Bull. Volcanol. *77*(8), 68, https://doi.org/10.1007/s00445-

662   015-0946-7.

663   Julian, B.R., 1994. Volcanic tremor: nonlinear excitation by fluid flow. J. Geophys. Res.

664   99, 11859-11877, https://doi.org/10.1029/93JB03129.

665   Kim, K., Lees, J.M., Ruiz, M.C., 2014. Source mechanism of Vulcanian eruption at

666   Tungurahua Volcano, Ecuador, derived from seismic moment tensor inversions. J. Geophys.

667   Res., Solid Earth 119, 1145-1164, https://doi.org/10.1002/2013JB010590.

668   Kolzenburg, S., Russell, J.K., 2014. Welding of pyroclastic conduit infill:

669   A mechanism for cyclical explosive eruptions, J. Geophys. Res., Solid Earth 119, 5305–5323,

670   https://doi.org/10.1002/ 2013JB010931.

671   Kumagai, H., Nakano, M., Maeda, T., Yepes, H., Palacios, P., Ruiz, M., Arrais, S., Vaca,

672   M., Molina, I., Yamashima, T., 2010. Broadband seismic monitoring of active volcanoes using

673   deterministic and stochastic approaches. J. Geophys. Res., Solid Earth *115*(B8),

674   https://doi.org/10.1029/2009JB006889.

675   Le Pennec, J.-L., Jaya, D., Samaniego, P., Ramón, P., Yánez, S.M., Egred, J., Van Der

676   Plicht, J., 2008. The AD 1300–1700 eruptive periods at Tungurahua volcano, Ecuador,

677   revealed by historical narratives, stratigraphy and radiocarbon dating. J. Volcanol. Geotherm.

678   Res. 176, 70-81, https://doi.org/10.1016/j.jvolgeores.2008.05.019.

679   Lesage, P., Mora, M.M., Alvarado, G.E., Pacheco, J., Métaxian, J.-P., 2006. Complex

680   behavior and source model of the tremor at Arenal volcano, Costa Rica. J. Volcanol.

681   Geotherm. Res. 157, 49-59, https://doi.org/10.1016/j.jvolgeores.2006.03.047.

682   Melnik, O., Barmin, A.A., Sparks, R.S.J., 2005. Dynamics of magma flow inside volcanic

683   conduits with bubble overpressure buildup and gas loss through permeable magma. J.

684   Volcanol. Geotherm. Res. 143, 53-68, https://doi.org/10.1016/j.jvolgeores.2004.09.010.

685   Mothes, P.A., Yepes, H.A., Hall, M.L., Ramón, P.A., Steele, A.L., Ruiz, M.C., 2015. The

686   scientific–community interface over the fifteen-year eruptive episode of Tungurahua Volcano,

687   Ecuador. *Journal of Applied Volcanology 4*(1), 9, https://doi.org/10.1186/s13617-015-0025-y.

688   Neuberg, J.W., Collinson, A.S., Mothes, P.A., Ruiz, M.C., Aguaiza, S., 2018.

689   Understanding cyclic seismicity and ground deformation patterns at volcanoes: Intriguing

690   lessons from Tungurahua volcano, Ecuador. Earth. Planet. Sci. Lett. *482*, 193-200,

691   https://doi.org/10.1016/j.epsl.2017.10.050.

692   Ripepe, M., Harris, A.J., Carniel, R., 2002. Thermal, seismic and infrasonic evidences of

693   variable degassing rates at Stromboli volcano. J. Volcanol. Geotherm. Res. 118, 285-297,

694   https://doi.org/10.1016/S0377-0273(02)00298-6.

695   Ripepe, M., Marchetti, E., Ulivieri, G., Harris, A., Dehn, J., Burton, M., Caltabiano, T.,

696   Salerno, G., 2005. Effusive to explosive transition during the 2003 eruption of Stromboli

697   volcano. Geology 33, 341-344, https://doi.org/10.1130/G21173.1.

698   Samaniego, P., Le Pennec, J.-L., Robin, C,, Hidalgo, S,, 2011. Petrological analysis of the

699   pre-eruptive magmatic process prior to the 2006 explosive eruptions at Tungurahua volcano

700   (Ecuador).   J.   Volcanol.   Geotherm.   Res.   199,   69-84,

701   https://doi.org/10.1016/j.jvolgeores.2010.10.010.

702   Vitturi, M.D.M., Clarke, A.B., Neri, A., Voight, B., 2008. Effects of conduit geometry on

703   magma ascent dynamics in dome-forming eruptions. *Earth Planet. Sci. Lett. 272*(3-4), 567-

704   578, https://doi.org/10.1016/j.epsl.2008.05.025.

705   Watt, S.F.L., Mather, T. A., Pyle, D.M., 2007. Vulcanian explosion cycles: Patterns and

706   predictability. Geology 35 (9), 839-842, doi:10.1130/G23562A.1.

707   Wright, H., Cashman, K., Mothes, P., Hall, M.L., Ruiz, A., and Le Pennec, J.-L., 2012.

708   Estimating rates of decompression from textures of erupted ash particles produced by 1999-

709   2006   eruptions   of   Tungurahua   volcano,   Ecuador.   Geology   40,   619-622,
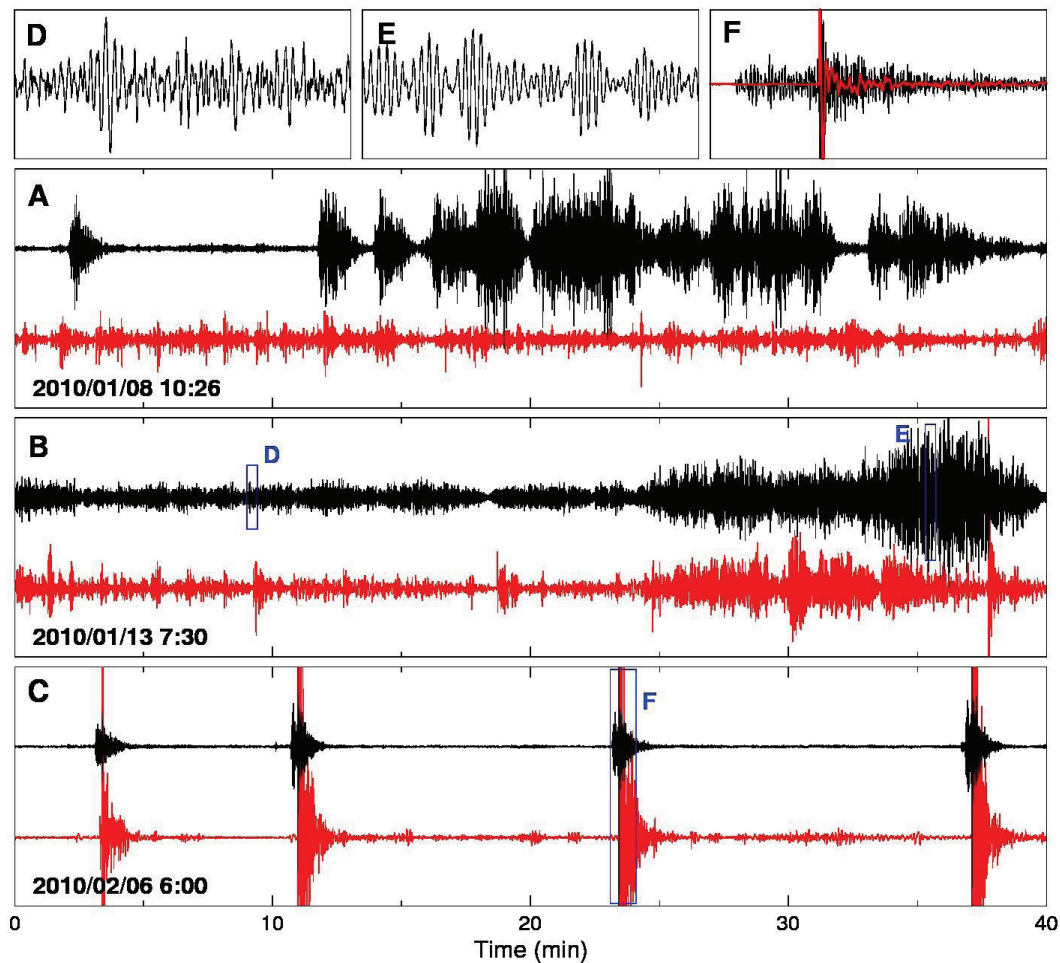
710   https://doi.org/10.1130/G32948.1.

711
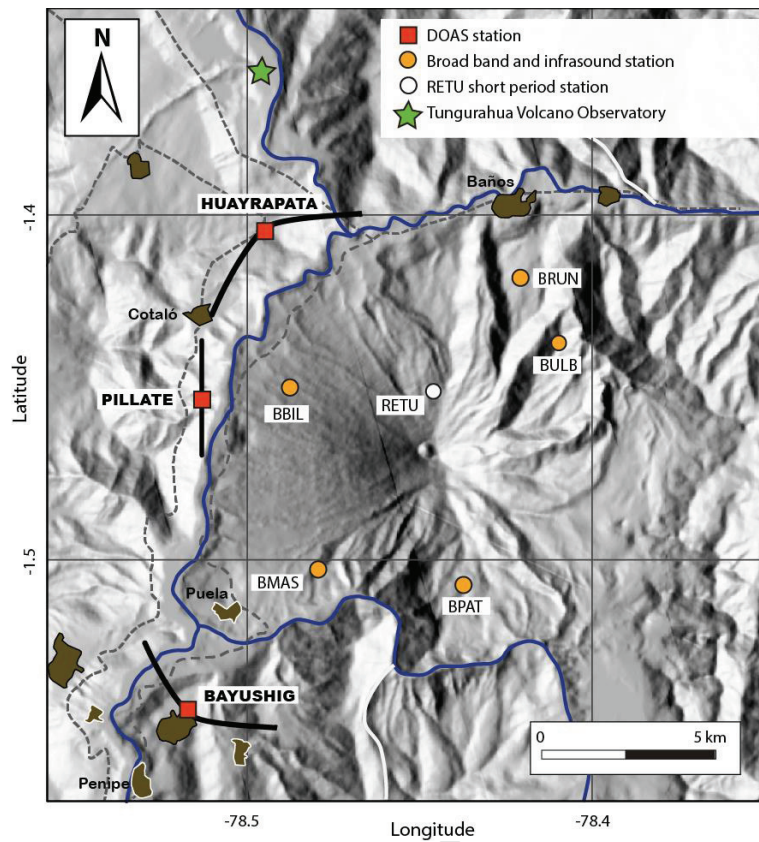
712
Figure 1: Map of Tungurahua volcano showing the location of the three scanning-DOAS
stations, five broadband seismic/infrasound stations and one1 short-period seismic station
RETU whose data was used for this study.

716
Figure 2: Seismic -vertical component- (black) and acoustic (red) signals recorded at station

BMAS. Plots (A), (B) and (C) show 40-min seismic and acoustic waveforms illustrating three

different types of eruptive activity starting at the times specified in the lower left corners. On

these 3 plots, seismic and acoustic traces have respectively common vertical scales and the

amplitude of acoustic traces have been divided by a factor 100. (A) Tremor bursts, mostly

harmonic, recorded during Strombolian activity in episode (b), (B) harmonic and non-

harmonic tremor bursts during episode (c) and (C) strong Vulcanian explosions and low

background tremor during episode (e). Plots (D) and (E) detail two 24-s windows showing

respectively examples of seismic recordings for non-harmonic and harmonic tremor. Plot (F)

shows a 60-s time frame for a seismic explosion quake with its corresponding acoustic signal.

727　All three time frames are extracted from the signals shown in plots (B) and (C) at the

728　corresponding locations shown within blue rectangles.

729

730
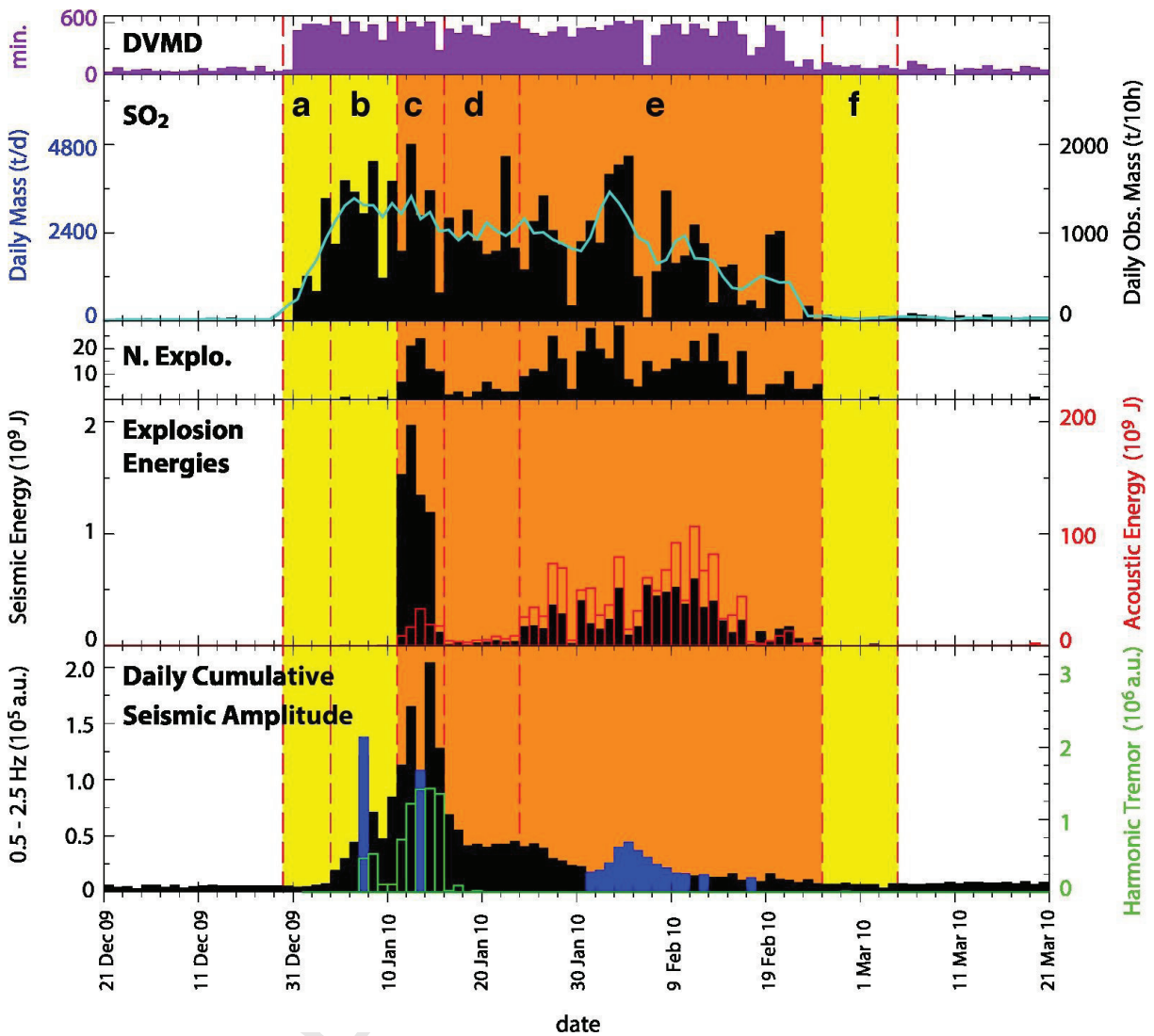
Figure 3: Comparison of geophysical time-series. Onset and ending times of the six episodes (a) to (f), described in the text, are delimited by vertical red dashed lines. HEA and LEA periods are displayed in yellow and orange background colors, respectively. "Daily Cumulated Seismic Amplitude" shows the daily cumulative values of the Median Seismic Amplitude (MSA) for the full short-period range at station RETU (black), completed with scaled data from BMAS (blue) when station RETU was down or saturated. "Explosions Energies" shows daily cumulative values of the seismic (black) and acoustic (red) energies for

738 the significant explosions. The vertical scale for acoustic energy is exactly 100 times that of

739 seismic so that the reader can directly compare the energies with respect to the threshold value

740 of 100 mentioned in the text. "N. Explo." displays the daily number of significant explosions.

741 "SO_2" shows the daily Observed Mass of SO_2 with the averaged values calculated over 5-d

742 sliding windows shown in turquoise. "DVMD" shows the Daily Valid Measurement Duration,

743 i.e. the number of minutes of valid SO_2 measurements. All three scanning-DOAS stations

744 were functioning properly during the study period. Figure 5 shows sketches presenting a

745 model of conduit dynamics corresponding to the six episodes.

746
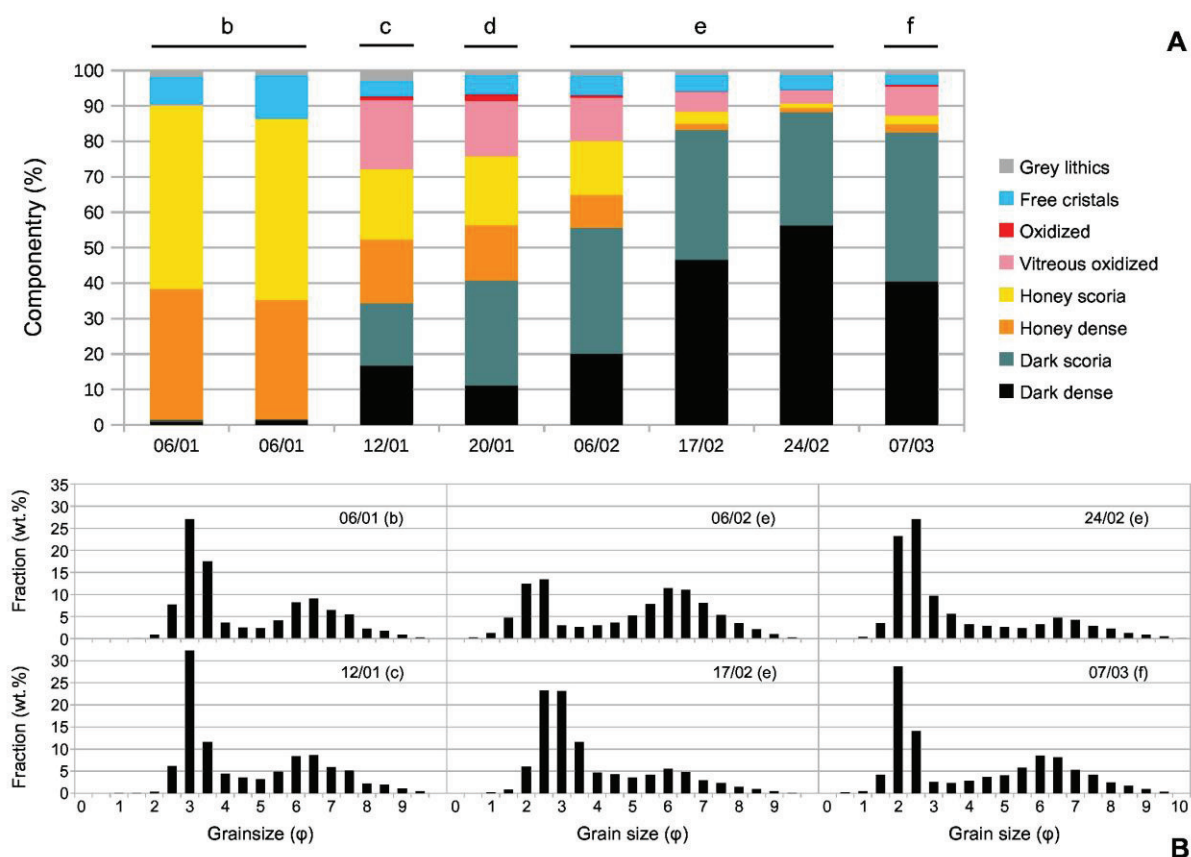
747
748 **Figure 4:** A) Barplots of the componentry and B) histograms of the grain-size distribution of

749 ash samples collected during the December 2009-March 2010 eruption. Description of the

750 components is given in the text. $\varphi = -\log_2 D$ where D is the particle diameter in millimeters. b,

751 c, d, e, f correspond to the eruptive episodes described in the text.
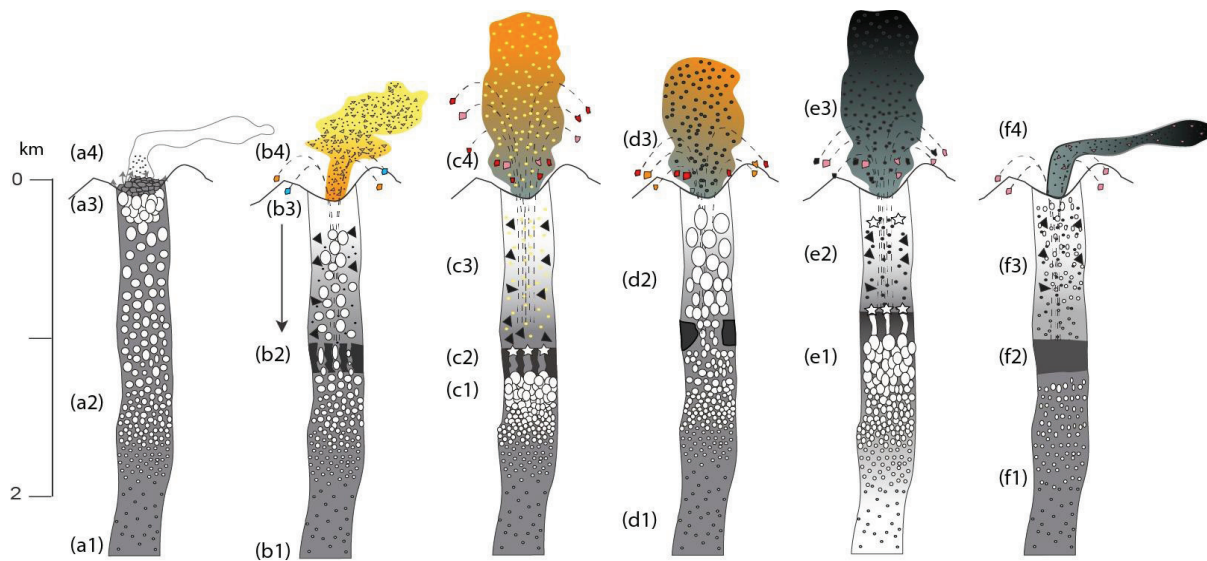
752
Figure 5: Sketches showing a model of conduit dynamics for the six episodes of activity defined in the text. Annotations along the sketches describe the characteristics of each activity from bottom to top. (a1) New magma input, (a2) gas easily exsolved, (a3) high gas pressure at the base of the lava accumulation in the crater, (a4) gas and ash venting. (b1) Steady arrival of magma, (b2) generation of a dense, gas depleted zone, (b3) destruction of the lava accumulation in the crater, (b4) gas and ash venting with Strombolian activity, emissions dominated by honey-color juvenile material. (c1) Gas accumulation below the dense zone, (c2) cyclical breaking of the dense zone, explosive release of gas, (c3) gas transport of juvenile material and cleaning of the conduit, (c4) gas and ash venting, Strombolian and Vulcanian activity. (d1) New magma injection with the same composition, (d2) mixed fragmentation process, (d3) steady ash column. (e1) same as (c2), (e2) gas transport of juvenile material with decreasing recycling, (e3) transition toward a more purely Vulcanian eruptive process. (f1) No more gas arrival, (f2) the dense zone cools down and forms a plug, (f3) remnant gas leaving the conduit, (f4) low gas and ash emission.